Initial-state and scattering-factor effects in photoelectron holography

S. Y. Tong, Hua Li, and H. Huang
Laboratory for Surface Studies and Department of Physics, University of Wisconsin–Milwaukee, Milwaukee, Wisconsin 53201
(Received 1 April 1994)

Angular anisotropies in the source wave and scattering factor are shown to cause artifacts in the images reconstructed from multiple-energy photoelectron holograms. A variable-axis small-angular-cone method is introduced to eliminate such anisotropies. We show that within the small angular cone, the anisotropy of the source wave towards an atom is canceled by that towards the detector. Also, the cone only samples the flat part of the slope of the scattering factor's phase. The remaining shift in the image position can be quantitatively corrected for the near-neighbor atoms.

In this paper, we demonstrate that angular anisotropies in the source wave and scattering factor can cause severe artifacts in the images reconstructed from photoelectron holograms. The situation is particularly serious for d and f initial-state core levels. A variable-axis small-angular-window method is introduced to eliminate the contributions from these angular anisotropies. Inversion of scan-energy photoelectron diffraction spectra within the variable-axis small angular cone then results in artifact-free images and the remaining shift in the atomic position can be quantitatively corrected for the near-neighbor atoms. Dynamical factors specific to the photoelectron diffraction process that can strongly distort the otherwise sinusoidal interference are (1) multiple scattering,[1–5] (2) angular anisotropy in the source wave, and (3) angular anisotropy in the electron-atom scattering factor.[6] Of the three, the contribution from multiple scattering can be eliminated by the use of multiple-wave-number photoelectron holograms.[2,5,7] An efficient method is to integrate a scan-energy photoelectron diffraction modulation over wave number:[5]

$$\phi_{\hat{k}}(\mathbf{R})=\int_{k_{\min}}^{k_{\max}}\chi(\mathbf{k})e^{-i(kR-\mathbf{k}\cdot\mathbf{R})}dk\ , \tag{1}$$

where $\chi(\mathbf{k})=I(\mathbf{k})/I_D(\mathbf{k})-1$ is a normalized energy-dependent photoelectron-diffraction (EDPD) spectrum in direction $\hat{k}$ and $I_D(\mathbf{k})$ is the reference (direct) intensity. The complex transform $\phi_{\hat{k}}(\mathbf{R})$ is summed over a set of closely spaced outgoing directions:[5]

$$\mu(\mathbf{R})=\left|\sum_{\hat{k}\in\Omega}\phi_{\hat{k}}(\mathbf{R})\right|^2 . \tag{2}$$

The reference intensity $I_D(\mathbf{k})$ cannot be measured directly; it is usually approximated by a least-square straight-line fit of $I(\mathbf{k})$ over a range of $(k_{\max}-k_{\min})$ at fixed θ_e and ϕ_e.[8] If the range in wave number is large, a least-square second-order polynomial fit is used.[9]

The action of the scan-energy transform defined in Eqs. (1) and (2) is to eliminate multiple-scattering contributions.[5] The scan-energy transform does not eliminate artifacts arising from angular anisotropies in either the source wave or the scattering factor. These anisotropies, both in the amplitude and phase, often cause troublesome artifacts in the reconstructed image. The artifacts appear as minima where the intensity should be maxima: peaks at nonatomic sites (i.e., false atoms), split peaks, and shifts in peak positions, etc.

As an illustration, we invert calculated EDPD spectra from Ga($3d$) in the Si(111) $\sqrt{3}\times\sqrt{3}$-Ga system. The surface structure of this system has been studied before by low-energy electron diffraction.[10] It is known that the Ga atom adsorbs at the T_4 hollow site. The EDPD spectra are calculated using a multiple-scattering slab method[11] in which the $d\rightarrow f$ and $d\rightarrow p$ dipole transition matrix elements are calculated at each energy. The incident photon is p polarized and the angle between the **A** vector and electron exit angle is held fixed at 20°. A mesh of EDPD spectra between $k_{\min}=2.85$ a.u.$^{-1}$ (110 eV) and $k_{\max}=4.8$ a.u.$^{-1}$ (313 eV) is used and the wave-number increment $\Delta k=0.075$ a.u.$^{-1}$. The EDPD spectra cover a large solid angle: from polar angle $\theta_e=0°$ (normal emission) to $\theta_e=85°$; the azimuthal angles cover a 60° sector from mirror plane to mirror plane and a C_{3v} operation is applied to the calculated spectra to span a 2π range. The crystal is rotated while keeping the angle between the **A** vector and detector fixed. The angular increments are $\Delta\theta_e=5°$ and $\Delta\phi_e=5°$.

The reconstructed images using Eqs. (1) and (2) over the full angular window are shown in Fig. 2, left panel.

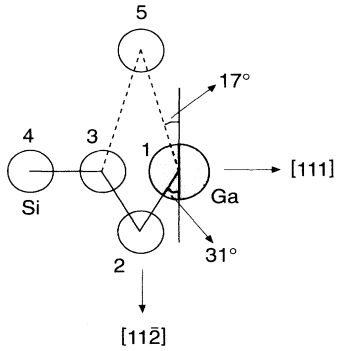

FIG. 1. Schematic diagram of the local structure.

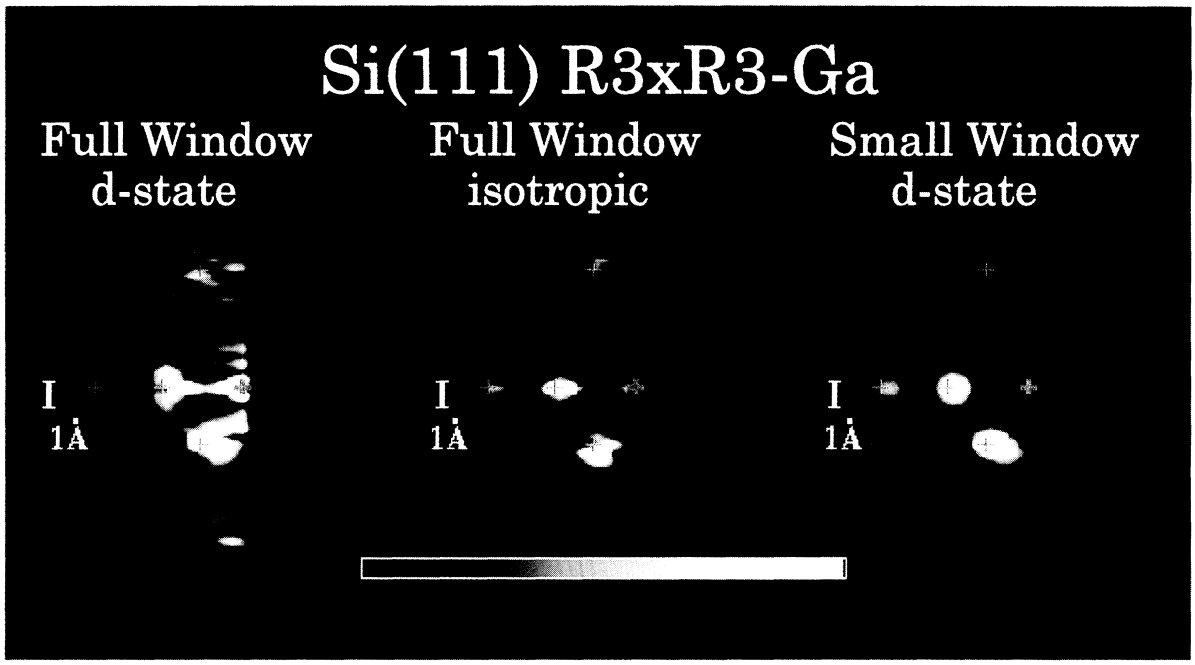

FIG. 2. Images of Si atoms 2–5 in Fig. 1.

The plane of view is normal to the surface and this plane passes through the Ga atom and Si atoms 2–5. Figure 1 shows the local cluster of the atoms in this plane. In Fig. 2, the crosses mark the positions of these atoms. We notice considerable artifacts in the picture, resulting in a generally high-noise background. Along the [111] direction, the images for Si(3) and Si(4) are severely distorted and minima appear where the crosses (atomic centers) are located. Very strong artifacts are seen at small radial distances from the emitter (thick cross). In an image reconstructed from a hologram, there should be no intensity at the source atom. A radial intensity plot from Ga to Si(3) and Si(4) is shown in Fig. 3, top panel. In this plot, the highest peak is at 0.3 Å and it is an artifact. The peak of Si(3) is shifted by 0.73 Å from the correct value of 2.57 Å (indicated by an arrow in the figure). Similarly, the peak of Si(4) is shifted by 0.72 Å from the correct value (second arrow). Referring back to Fig. 2, left panel, the image of Si(2) is split and a high-intensity streak is seen extending from this atom to small radial values. The image of Si(5) cannot be located because of considerable artifacts nearby. Generally speaking, this amount of artifacts in the reconstructed image is unacceptable.

Since multiple-scattering artifacts are already eliminated by the scan-energy transforms, the artifacts in Figs. 2 and 3 must be produced either by the angular anisotropy in the source wave or in the scattering factor. To separate the two effects, we replace the $d \rightarrow f$ and $d \rightarrow p$ source terms by an s-wave source term in the calculation. It should be recognized that an s-wave source term does not exist in real systems because of the dipole selection rule. Therefore, it is purely a theoretical construction. However, the construction is valuable because it separates source-wave-induced artifacts from scattering-factor-induced artifacts.

The reconstructed images and radial distribution plot using an s-wave source term while keeping all other conditions the same as before are shown, respectively, in the center panels of Figs. 2 and 3. Since all other conditions are the same, any difference between the left and center panels of Fig. 2 or top and center panels of Fig. 3 is due to source-term-induced artifacts. There are indeed con-

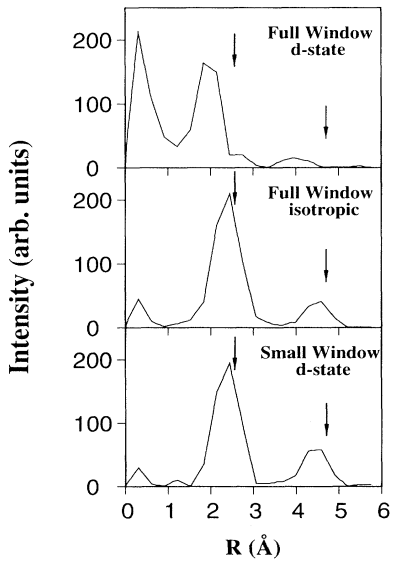

FIG. 3. Radial intensity scan from Ga to Si(3) and Si(4). Arrows mark the correct atomic positions.

siderable differences: the images are much sharper—most of the artifacts in the background, especially those at small radial values, are gone. The distortions and splittings in Si(3) and Si(4) are eliminated. The resulting single-maximum images have a resolution of less than 1 Å. The radial intensity plot (Fig. 3, center panel) shows that the image of Si(3) is at 2.451 Å, shifted by only 0.119 Å from the correct value. The peak for Si(4) is at 4.595 Å, shifted only by 0.115 Å. The images in Fig. 2, center panel, are almost perfect except for badly split images for Si(2) and Si(5). The splitting of Si(2) and Si(5) and the shift in the image position must be scattering-factor induced. But why are the images of Si(2) and Si(5) split while those of Si(3) and Si(4) are not? And why does the source wave cause the other artifacts? To answer these questions, we must examine the functional forms of the source wave and scattering factor.

The normalized scan-energy EDPD can be written as[5]

$$\chi(\mathbf{k}) \sim \cdots + f_k(\hat{\mathbf{k}}\cdot\hat{\mathbf{R}}_1)F_k(\hat{\mathbf{R}}_1)F_k^{-1}(\hat{\mathbf{k}})\frac{e^{i(kR_1-\mathbf{k}\cdot\mathbf{R}_1)}}{R_1}+\cdots, \tag{3}$$

where $\mathbf{R}_1$ is the position of a silicon atom measured from the source atom (Ga). The scattering factor of silicon is $f_k(\hat{\mathbf{k}}\cdot\hat{\mathbf{R}}_1)$, $\hat{\mathbf{k}}$ is the direction of the EDPD, and $F_k(\hat{\mathbf{k}})$ is the source wave in direction $\hat{\mathbf{k}}$. The origin of the coordinated system is at the Ga atom. Only the single-scattering term is shown explicitly in Eq. (3) because multiple-scattering contributions are eliminated by Eqs. (1) and (2). The source wave is given by[11,12]

$$F_k(\hat{\mathbf{k}})=\frac{1}{k}\sum_L i^{-(l+1)}Y_L(\hat{\mathbf{k}})A_L\ , \tag{4}$$

where the vector A_L is obtained from the dipole-excitation

$$A_l=(-i)^l\int d^3r e^{i\delta_l}R_f^f(r)Y_L^*(\hat{r})\frac{i\hbar e}{mc(E_f-E_i)} \times \mathbf{A}\cdot\nabla V(r)\sum_{L_i}C_{L_i}R_{l_i}^i(r)Y_L(\hat{r})\ . \tag{5}$$

In Eq. (5), $R_{l_i}^i(r)$ and $R_l^f(r)$ are radial solutions to the Ga potential at initial- and final-state energies E_i and E_f, respectively, $\mathbf{A}\cdot\nabla V(r)$ is the dipole excitation operator. The final-state angular momenta are given by the selection rule

$$L=(l,m)=(l_i\pm1\ ;\ m_i\ ,\ m_i\pm1)\ . \tag{6}$$

For the d-core level of Ga, the five initial states produce five independent source waves. The measured intensity is an incoherent sum of the contributions for each initial state. If the factor $f_k(\hat{\mathbf{k}}\cdot\hat{\mathbf{R}}_1)F_k(\hat{\mathbf{R}}_1)F_k^{-1}(\hat{\mathbf{k}})$ in Eq. (3) is independent of $\hat{\mathbf{k}}$, then the single-scattering term is a sinusoidal function over $\hat{\mathbf{k}}$ and this corresponds exactly to a Gabor-type optical hologram. In reality, $f_k(\hat{\mathbf{k}}\cdot\hat{\mathbf{R}}_1)$, $F_k(\hat{\mathbf{R}}_1)$, and $F_k^{-1}(\hat{\mathbf{k}})$ all have strong angular anisotropies, in their amplitudes and phases. We show in Fig. 4 the angular dependences of $F_k(\hat{\mathbf{k}})$ for the phase (left panels) and the amplitude (right panels). The five source waves,

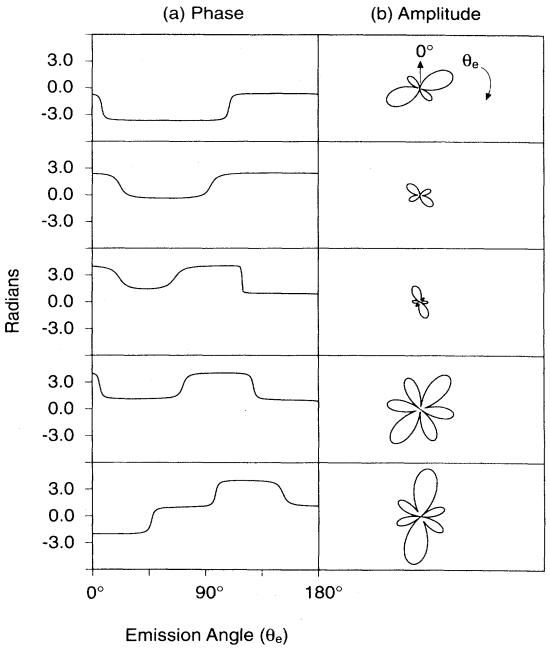

FIG. 4. The five source waves at photoelectron energy 110 eV and d-initial states (from bottom to top): $3z-r^2$, xz, yz, xy, and x^2-y^2, respectively. For the top two states, the phase jumps by π just beyond 180°.

evaluated by Eqs. (4) and (5) for oriented d orbitals, are shown as functions of the polar emission angle θ_e. The azimuthal emission angle is fixed at 15° from the x axis and the photon $\mathbf{A}$ vector is pointed at 30° from the z axis and its projection in the xy plane has an azimuthal angle of 45°. We note that the five source waves are rapidly varying functions of angles. The matter is worst at angles where the amplitude of $F_k(\hat{\mathbf{k}})$ is at a cusp, since its phase jumps through values of near π. If we expand the phase of $F_k(\hat{\mathbf{k}})$ in a polynomial function over wave number k, at the angles where the phase jumps through near π, its functional form is highly nonlinear. While the linear coefficient in the expansion produces a shift in the image position,[13] the nonlinear coefficients produce distortions and splittings that are not easily predicted.

Given the strong angular anisotropies in the amplitude and phase of $F_k(\hat{\mathbf{k}})$ and that an ideal s-wave source term does not exist, is there then a method to invert a distorted hologram? Fortunately, a solution does exist. From Eq. (4), we note that since the parity of $Y_L(\hat{\mathbf{k}})$ is l, then the following relation is true:[14,15]

$$F_k(\hat{\mathbf{R}})=(-1)^{l_i+1}F_k(\hat{\mathbf{k}}) \tag{7}$$

provided $\hat{\mathbf{R}}=-\hat{\mathbf{k}}$. In other words, for a given $\hat{\mathbf{R}}$ direction, if we restrict the wave-number transform and sum over EDPD's to within a small angular cone *whose central axis is along the* $-\hat{\mathbf{R}}$ *direction,* then whenever $\hat{\mathbf{R}}$ points along an atomic direction $\hat{\mathbf{R}}_1$, the factors $F_k(\hat{\mathbf{R}}_1)$ and $F_k^{-1}(\hat{\mathbf{f}})$ cancel up to a constant $(-1)^{l_i+1}$. This means the source-wave anisotropy is reduced or even

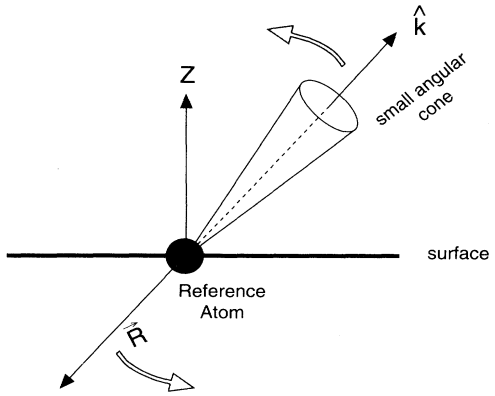

FIG. 5. Variable-axis SWEEP.

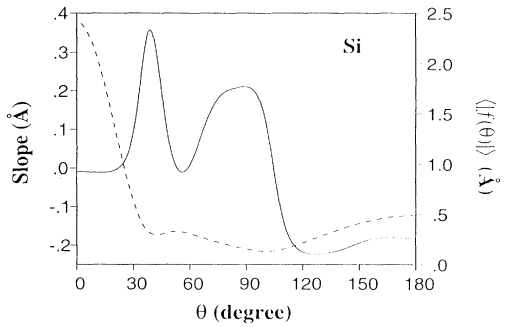

FIG. 6. The slope (solid curve) and average amplitude (dashed curve) in the k range 2.85 to 4.8 a.u.$^{-1}$.

completely eliminated within the small angular cone. The method is a variation of the small-window energy-extension process (SWEEP) introduced earlier,[1,2] but here, for each $\mu(\hat{\mathbf{R}})$ in Eq. (2), a different small window is used. $\hat{\mathbf{R}}$ remains a variable sweeping over all real space. A schematic picture of the variable-axis SWEEP (VASWEEP) method are shown in Fig. 5.

Results of the VASWEEP method are shown in Fig. 2, right panel and Fig. 3, lower panel, respectively. The half-angular opening of the cone used is 25°. The Ga $d\rightarrow f$ and $d\rightarrow p$ source terms are restored in the calculation. Looking at the images for Si(3) and Si(4), the quality is good and similar to that achieved in the s-wave construction. This is an indication that within the small angular cone, the cancellation between $F_k(\hat{\mathbf{R}}_1)$ and $F_k^{-1}(\hat{\mathbf{k}})$ is almost complete. The images have a more rounded appearance because of the loss of resolution in the direction parallel to the surface. This is because the range in $\Delta\mathbf{k}_{\parallel}$ is restricted in the small window. However, the resolution in all directions is near 1 Å. The radial intensity plot (Fig. 3, bottom panel) is also almost identical to the s-wave case—the peak positions of Si(3) and Si(4) are, respectively, shifted by 0.119 and 0.115 Å as before, indicating that these shifts are caused by the scattering factor and not the source wave.

The right panel of Fig. 2 shows another improvement: the images of Si(2) and Si(5) are no longer split. To understand this, we recall from Eq. (3) that after the cancellation of the source terms, the single-scattering expression of $\chi(\mathbf{k})$ contains only $f_k(\hat{\mathbf{k}}\cdot\hat{\mathbf{R}}_1)$ as its coefficient. Again, by expressing $f_k(\hat{\mathbf{k}}\cdot\hat{\mathbf{R}}_1)$ in terms of its amplitude and phase: $f_k(\hat{\mathbf{k}}\cdot\hat{\mathbf{R}}_1)=f_k(\theta)=|f_k(\theta)|e^{i\phi_k(\theta)}$ and expanding the phase in a polynomial over k, we obtain

$$\phi_k(\theta)=\alpha(\theta)+\beta(\theta)k+\gamma(\theta)k^2+\cdots . \quad (8)$$

In Fig. 6, we plot the linear coefficient $\beta(\theta)$ vs scattering angle (left ordinate) and the average amplitude $\langle|f(\theta)|\rangle=\sum_{k=1}^{N}|f_k(\theta)|/N$ (right ordinate) over the wave-number range considered. The linear coefficient (i.e., slope) is a rapidly varying function of θ, except at the forward ($\theta=0°-20°$) and back ($\theta=155°-180°$) scattering regimes where it is flat. In the VASWEEP method, as $\mathbf{R}$ sweeps through all points of real space, only EDPS's in the near π scattering region are included. This means only scattering factors $f_k(\theta)$ for $\theta\approx\pi$ are sampled. Because the average amplitude $\langle|f(\theta)|\rangle$ and slope $\beta(\theta)$ in the near π region are slowly varying or flat, the single-scattering term of $\chi(\mathbf{k})$ behaves exactly like a Gabor-type optical hologram. Therefore, the reconstructed image should be free of artifacts. The only remaining correction is a shift in the image position due to the slope $\beta(\theta)$.

It is important to realize that the advantage of using a near π small angular cone is to sample a region of $f_k(\theta)$ where the slope of its phase is flat. Indeed, it is secondary whether the amplitude at near π is large or not. From Fig. 6, the amplitude of $f_k(\theta)$ averaged over the energy range is only mildly varying from 90° to 180°. It is also serendipitous that in the near π region where the angular anisotropies of the source terms cancel each other, this same region contains the flat part of the slope of $f_k(\theta)$ phase.

With the behavior of the slope $\beta(\theta)$ known (see Fig. 6), it is simple to understand why in the full-window s-wave case (middle panel, Fig. 1) the images of Si(2) and Si(5) are split while those of Si(3) and Si(4) are not. For Si(3) and Si(4), using EDPD's in the full window means that the scattering angle of $f_k(\theta)$ sampled is from $\theta=95°$ to 180°. The slope $\beta(\theta)$ varies comparatively little in this region. On the other hand, for Si(2) using the full-window samples θ from 36.4° to 206.4°. From Fig. 6, the slope $\beta(\theta)$ fluctuates from positive to negative values in this region. Similarly, for Si(5), the angular range sampled is 22° to 192°, where again $\beta(\theta)$ undergoes a large fluctuation. It is known that large fluctuations in the sign of the slope cause the reconstructed image to split (see the explanation given in Ref. 6). In the VASWEEP method, on the other hand, the sampling of $\beta(\theta)$ is always restricted to the near π region where it is flat. The images, therefore, are never split.

Because of the near linear dependence of the scattering phase on the wave number in the near π region, it is possible to quantitatively correct for the remaining shift in the image position, at least for the near-neighbor atoms. From Eqs. (1) and (3), again assuming the cancellation of the source terms, the wave-number transform produces an image at

$$R=\frac{R_1(1-\cos\theta)+\beta(\theta)}{(1-\cos\theta)} . \quad (9)$$

The average scattering angle is 180° within the cone, and $\beta(\pi)=-0.182$ Å from Fig. 6. Therefore, using $R=2.451$ Å from Fig. 3, bottom panel for Si(3), we obtain $R_1=2.542$ Å, which is less than 0.03 Å from the correct value. A precision of 0.03 Å is comparable to that of the best (indirect) diffraction methods.

Fadley and co-workers[16] have studied the scanned energy and scanned angle variants of holographic inversion. In the scanned-energy version, they used a fine energy mesh and a coarse angular mesh and vice versa for the scanned-angle version. They neglected differences in the reference wave in the two versions. The present work shows that the best method is to use a fine energy mesh and a fine angular mesh. Also, the angular range should be restricted to a small opening. This is because fine meshes in both energy and angle are needed to eliminate multiple-scattering artifacts, while a small angular opening is needed to suppress anisotropies in the source wave and scattering factor. Finally, the splitting in the images of Si(2) and Si(5) is due to fluctuations in the slope of the scattering-factor's phase as a function of angle. It is not related to the generalized Ramsauer-Townsend resonances.[17]

In conclusion, we have shown why it is important to eliminate distortions caused by the angular anisotropies of the source wave and scattering factor in a photoelectron hologram. We have introduced a variable-axis SWEEP method which reduces a distorted photoelectron hologram to a Gabor-type optical hologram within the small angular cone. Inversion of the hologram then results in mostly artifact-free images and the remaining shift in the atomic position of the near-neighbor atoms can be quantitatively corrected by the average slope of the scattering-factors phase. We recently became aware that Wu and Lapeyre[18] have developed a process similar to our variable-axis SWEEP method.

This work is supported by the National Science Foundation, Grant No. DMR-9214054. Computation was carried out at the National Center for Supercomputing Applications (NCSA).

[1]H. Huang, Hua Li, and S. Y. Tong, Phys. Rev. B **44**, 3240 (1991)

[2]S. Y. Tong, H. Huang, and Hua Li, in *Advances in Surface and Thin Film Diffraction,* edited by T. C. Huang, P. I. Cohen, and D. J. Eaglesham, MRS Symposia Proceedings No. 208 (Materials Research Society, Pittsburgh, 1991), p. 13; S. Y. Tong, Hua Li, and H. Huang, Phys. Rev. Lett. **67**, 3102 (1991).

[3]S. A. Chambers, V. A. Loobs, Hua Li, and S. Y. Tong, J. Vac. Sci. Technol. B **10**, 2092 (1992).

[4]S. A. Chambers, Surf. Sci. Rep. **16**, 261 (1992), and references therein.

[5]S. Y. Tong, H. Huang, and C. M. Wei, Phys. Rev. B **46**, 2452 (1992).

[6]S. Y. Tong, H. Li, and H. Huang, Phys. Rev. B **46**, 4155 (1992).

[7]J. J. Barton, Phys. Rev. Lett. **67**, 3106 (1991).

[8]J. G. Tobin, G. D. Waddill, H. Li, and S. Y. Tong, Phys. Rev. Lett. **70**, 4150 (1993).

[9]H. Wu, G. J. Lapeyre, H. Huang, and S. Y. Tong, Phys. Rev. Lett. **71**, 251 (1993).

[10]A. Kawazu and H. Sakama, Phys. Rev. B **37**, 2704 (1988).

[11]C. H. Li and S. Y. Tong, Phys. Rev. B **19**, 1769 (1979).

[12]S. Y. Tong, H. C. Poon, and D. R. Snider, Phys. Rev. B **32**, 2096 (1985).

[13]S. Y. Tong, C. M. Wei, T. C. Zhao, H. Huang, and Hua Li, Phys. Rev. Lett. **66**, 60 (1991).

[14]S. Y. Tong and J. C. Tang, Phys. Rev. B **25**, 6525 (1982).

[15]V. Fritzsche, R. Davis, X. M. Hu, D. P. Woodruff, K. U. Weiss, R. Dippel, K. M. Schindler, Ph. Hofmann, and A. M. Bradshaw, Phys. Rev. B **49**, 7729 (1994).

[16]C. S. Fadley, in *Applications of Synchroton Radiation Techniques to Materials Science,* edited by D. L. Perry, N. Shinn, R. Stockbauer, K. D'Amico, and C. Terminello, MRS Symposia Proceedings No. 307 (Materials Research Society, Pittsburgh, 1993), p. 261.

[17]J. J. Barton, Z. Hussain, and D. A. Shirley, Phys. Rev. B **35**, 933 (1987).

[18]H. Wu and G. J. Lapeyre (unpublished).

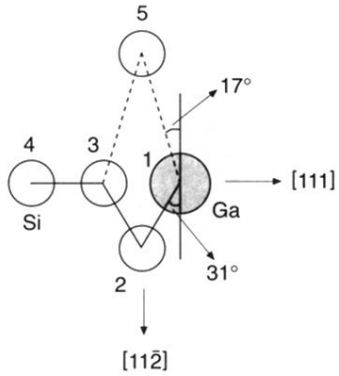

FIG. 1. Schematic diagram of the local structure.

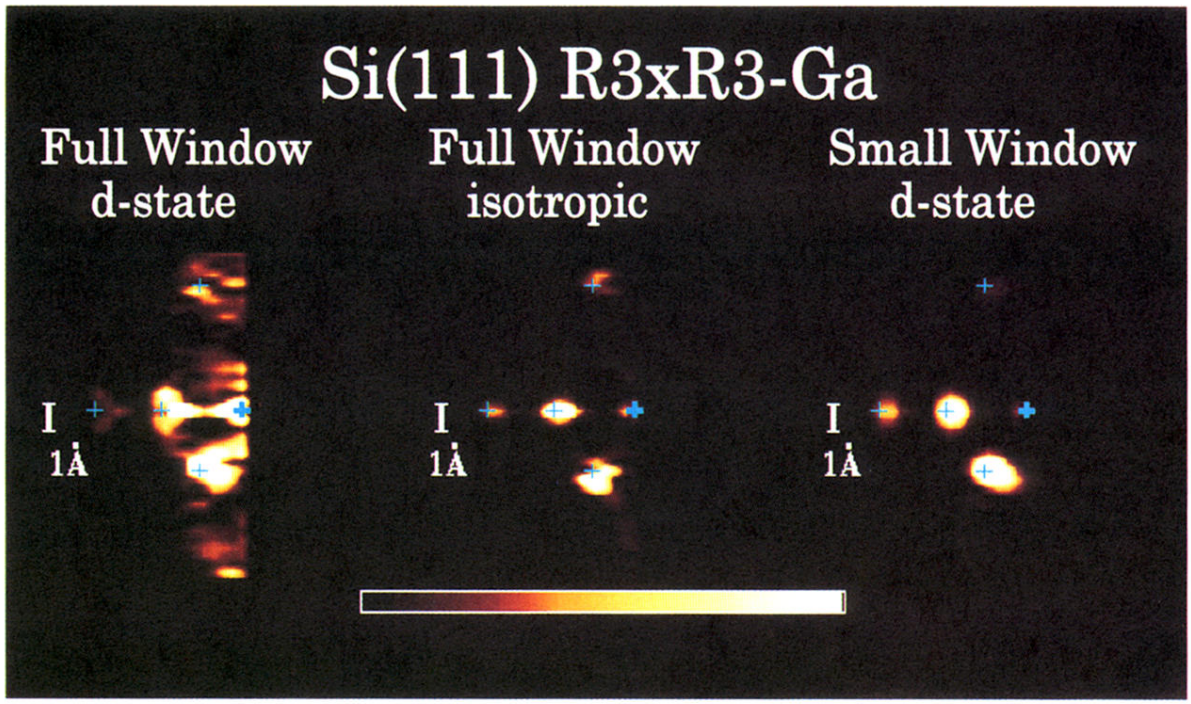

FIG. 2. Images of Si atoms 2–5 in Fig. 1.